JMEPEG (2011) 20:1330–1335
DOI: 10.1007/s11665-010-9769-z

1059-9495/$19.00

Characterization of Corrosion Product Layers from CO_2 Corrosion of 13Cr Stainless Steel in Simulated Oilfield Solution

Z.F. Yin, X.Z. Wang, L. Liu, J.Q. Wu, and Y.Q. Zhang

(Submitted July 8, 2009; in revised form September 14, 2010)

The influence of temperature and flow rate on the characterization and mechanisms of corrosion product layers from CO_2 corrosion of 13Cr stainless steel was carried out in simulated oilfield solution. Cyclic potentiodynamic polarization method as well as weight loss tests in autoclave were utilized to investigate pitting corrosion behavior at various temperatures. Weight loss tests were performed at 100 and 160 °C under dynamic and static flow conditions. At the same time, the significant pitting parameters such as E_{corr}, E_{pit}, E_{pp}, ΔE, and I_{pass} in cyclic polarization curves at various temperatures were analyzed and compared for revealing the pitting behavior of 13Cr stainless steel. The surface measurement techniques such as SEM, XRD, and XPS were used to detect the corrosion product layers. The results showed that both temperature and flow rate had significant effects on characterization of corrosion product layers or passive films formed on 13Cr stainless steel in CO_2 corrosion system. At high temperature, lots of pits were formed at the localized corrosion areas of metal surfaces. Corrosion rates under the condition of 5 m/s were higher than those under the static condition regardless of the test temperatures.

Keywords 13Cr stainless steel, CO_2 corrosion, corrosion product layers, flow rate, XPS

1. Introduction

In the oil industry a very serious concern is CO_2 corrosion, which can be generalized or localized, depending on the corrosion environments. In general, the type of localized corrosion results from the aqueous solution saturated with CO_2 and containing chloride in the oil and gas production (Ref 1, 2). The corrosive aggressiveness is directly related to the variables such as material compositions, temperature, flow characteristics, pH, water composition, CO_2 partial pressure, and passive films or corrosion product films (Ref 3, 4).

Due to better corrosion resistance in CO_2 environment and lower cost compared with other stainless steels such as duplex stainless steel, 13Cr stainless steel was widely used in oil and gas field containing CO_2 (Ref 5-7). For the role of a passive film on stainless steel, in general, a few nanometer thick film rich in chromium is expected to inhibit corrosion (Ref 8, 9). Some studies (Ref 10-13) have reported that temperature plays a significant role in the corrosion resistance of 13Cr stainless steel. In CO_2 corrosive media, 13Cr stainless steels present a good corrosion resistance as long as the temperature does not exceed 150 °C (Ref 12, 13).

In addition, flow can influence CO_2 corrosion based on whether the protective film forms. The flow acceleration effect can be attributed to the flow-sensitive nature of cathodic reactions. For instance, H^+ reduction is very flow sensitive at the low H^+ concentrations and the reduction of H_2CO_3 is less flow-sensitive than H^+ reduction reaction in CO_2 corrosion (Ref 14).

The promotion of pit formation in the passive film by the most significant anions such as Cl^- ion has been described in many publications (Ref 15-17). Ikeda et al. (Ref 18) considered that the amount of chloride is greater than 50,000 ppm, 13Cr stainless steels will generally be subject to pitting corrosion. It is generally believed that micro-pits are stabilized by the precipitation of a salt layer at its bottom. The passive films with weak stresses are more desired for repassivated while sound compact films tend to protect the pits from being repassivated (Ref 19). Wilde and Willianms (Ref 20) showed that it is more difficult to repassivate pits when they grow deeper.

In this article, the characterization of corrosion product layers from CO_2 corrosion on 13Cr stainless steel in simulated oilfield solution was studied by weight loss, SEM, XRD, and XPS measurement methods, as well as the electrochemical corrosion behavior. We aim to gain a further understanding about the influence of temperature and flow rate on the corrosion characterization and pitting mechanisms of 13Cr stainless steel in simulated oilfield solution containing high Cl^- ions under the dynamic and static flow conditions.

2. Experimental

2.1 Weight Loss Measurements

The samples for weight loss tests are 13Cr stainless steel slices, with a size of $40 \times 10 \times 3$ mm, whose chemical composition were (wt.%): C 0.19, Si 0.32, Mn 0.44, P 0.0016, S 0.032, Cr 13.13, Mo 0.072, Ni 0.12, Cu 0.01, Fe

Z.F. Yin, X.Z. Wang, L. Liu, J.Q. Wu, and **Y.Q. Zhang**, Shaanxi Yanchang Petroleum Group Company, Petroleum Research Institute, Xi'an, Shaanxi, China. Contact e-mail: yinzhifu919@sohu.com.

Balance. All samples surfaces were mechanically polished by emery sandpaper progressively up to 800 grades, then degreased with acetone and rinsed with absolute alcohol, weighted with 0.1 mg precision, finally put in the high-temperature and high-pressure autoclave made by Cortest (USA). Prior to the tests, the pure N_2 was poured forcedly into the solution and bubbled for 12 h before the introduction of CO_2 gas. The temperatures were, respectively, controlled at 100 and 160 °C under the dynamic (5 m/s) and static flow conditions. In addition, the system was pressured with CO_2 gas to the partial pressure of 4 MPa. The immersion tests were carried out for 120 h in the simulated oilfield solution, which was composed of deionized water and main ions with the concentrations of Cl^- 50 g/L, SO_4^{2-} 1.5 g/L, HCO_3^- 0.8 g/L, Ca^{2+} 0.5 g/L, and Mg^{2+} 1.5 g/L. After each test, the samples were rinsed with distilled water and absolute alcohol, and then they were divided into two groups: the samples in group one were descaled with Clark solution (20 g Sb_2O_3 + 50 g $SnCl_2$ + 1 L HCl), then the weight loss was measured; The samples in group two were not descaled, which were dried and stored in desiccator until analysis.

2.2 SEM, XRD, and XPS analyses

Corrosion product layers on the corroded samples were analyzed using PHI-5400 ESCA XPS system with a set of experimental parameters as follows: a MgKα x-ray source with a power of 400 W, a pass energy of 89.450 eV for narrow scan, an analysis area approximately 0.8 mm^2 and a vacuum in the test chamber of 2×10^{-8} Pa. The binding energies (BEs) were calibrated by taking C1s peak, 284.6 eV as a criterion. XRD experiment was performed using Japan D/Max-2400 automatic x-ray diffraction apparatus with CuKα x-ray source, an accelerating voltage of 40 kV and a current density of 40 mA/cm^2. Scanning electron microscopy (SEM) was utilized to investigate micro-morphology of the corrosion scale. Before SEM, XRD, and XPS experiments, the samples were cleaned in acetone to remove the surface contamination.

2.3 Electrochemical Measurement

Cyclic potentiodynamic polarization measurements were carried out in a conventional three-electrode cell. The counter electrode was a pair of graphites with a saturated calomel electrode (SCE) working as the reference electrode. All potentials were referred to SCE. An EG&G Princeton Research (PAR) Model 273A potentiostat/galvanostat controlled by a personal computer were used. Cyclic potentiodynamic polarization was performed by starting from a negative potential at −100 mV of E_{corr} with a sweep rate of 0.2 mV/s. In electrochemical tests, the rod samples (∅ 15 mm × 5 mm) were mounted into epoxy resin leaving a working area of 1.767 cm^2.

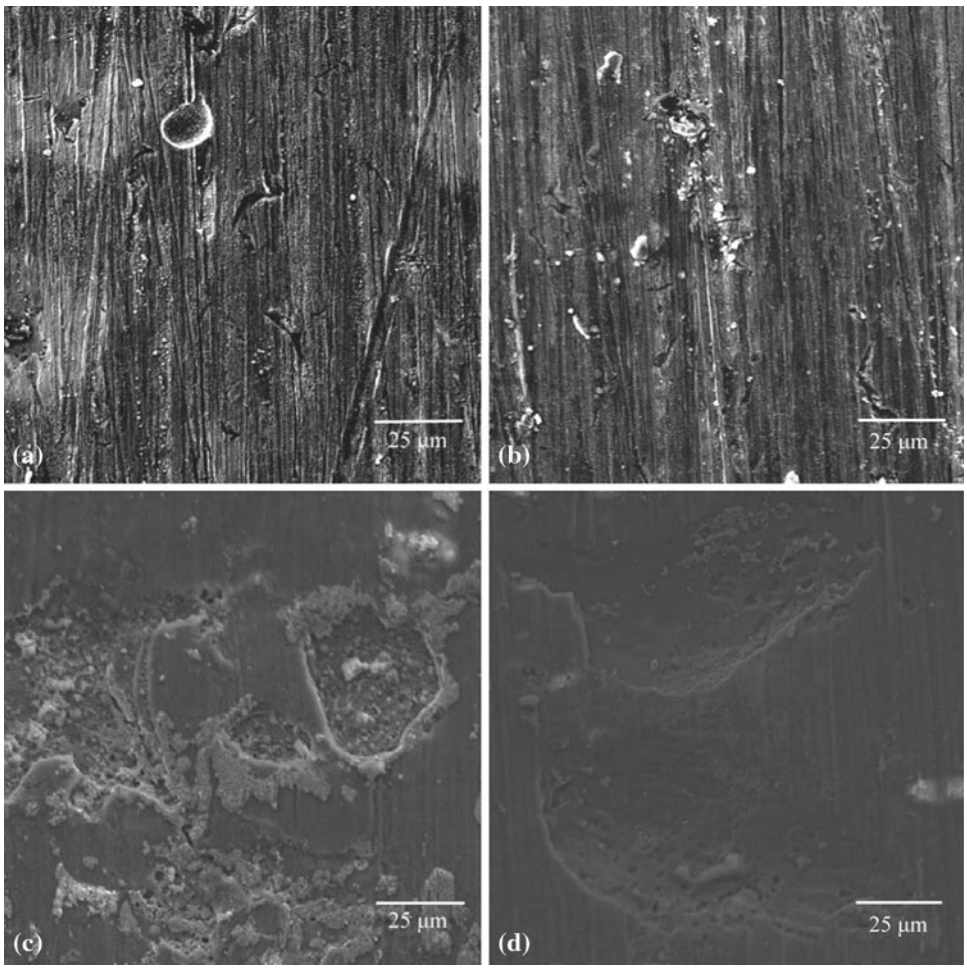

Fig. 1 Surface morphologies of corrosion product layers formed at different temperatures and flow rates: (a) 5 m/s + 100 °C, (b) 0 m/s + 100 °C, (c) 5 m/s + 160 °C, and (d) 0 m/s + 160 °C

Before experiments, the simulated oilfield solution was deaerated by pure nitrogen for 1 h and then CO_2 was bubbled in solution for 0.5 h, respectively. During the experiments, CO_2 was bubbled successively through the solution. The test temperatures were controlled at 30, 60, and 90 °C, respectively.

3. Results and Discussion

3.1 SEM Observation and Weight Loss Measurement

Figure 1 shows the surface morphologies of corrosion product layers formed at different temperatures under dynamic and static flow conditions. It is worthwhile to mention that the surface microstructures of the corroded samples formed at 100 °C are obvious different from those formed at 160 °C regardless of the dynamic flow or static conditions. Some individual pits were observed on metal surfaces at 100 °C. The aggressive species such as Cl^- ions rapidly transfer to the metal surface and some sites of local corrosion product layers with defects are first attacked, and then some sites will nucleate and grow; however, some micro-pits will be repaired and repassivated. The similar mechanisms were reported in many literatures (Ref 21, 22). Compared to the corrosion morphologies formed at 100 °C, severe localized corrosion (i.e., the corrosion product layers are peeled away at 160 °C) occurs on the metal surfaces and where large numbers of corrosion pits are formed as shown in Fig. 1(c) and (d). It is attributed to the effect of high concentration of Cl^- ions and high temperature (160 °C). When the temperature reaches 160 °C, the passive film and/or the corrosion product layers are relatively stable, so some formed micro-pits are not easy to repair and continue to nucleate and grow with the effect of high Cl^- concentration. In general, Cl^- ion has two influences on steel surfaces during CO_2 corrosion. On the one hand, increasing Cl^- concentrations will reduce the corrosion rate due to the reducing solubility of CO_2 gas in aqueous solution (Ref 23). On the other hand, the addition of Cl^- ions will diminish the formation trend of passive films or accelerate the cracking of passive films, both of which result in the serious attack (Ref 24, 25). It is observed that some sites near the damaged corrosion product layers are covered by one layer of salt sediment produced from the test solution.

Figure 2 shows that the corrosion rates (CR) of 13Cr stainless steel are about 0.082 mm/a (dynamic flow) and 0.057 mm/a (static flow) at 100 °C compared with 0.468 mm/a (dynamic flow) and 0.408 mm/a (static flow) at 160 °C, which are calculated by weight loss method. The corrosion rate increases about 5-7 times when temperature increases from 100 to 160 °C. This result indicates that 13Cr stainless steels present a reduced corrosion resistance when temperature exceeds 150 °C, which is in accordance with the research by Miyata et al. (Ref 12) and Kermani et al. (Ref 13). In addition, it can be found that the CR in the case of 5 m/s is higher than that in static condition at 160 °C, as well as the result at 100 °C. Because the corrosion product layer formed at 100 °C is insufficiently protective, the turbulent flow is to enhance transport of aggressive species toward and away from the steel surface leading to an increase in corrosion rate. When temperature is controlled at 160 °C, the corrosion product layers are thickened and more compact, to some degree, which can inhibit corrosion due to formation of the protective films.

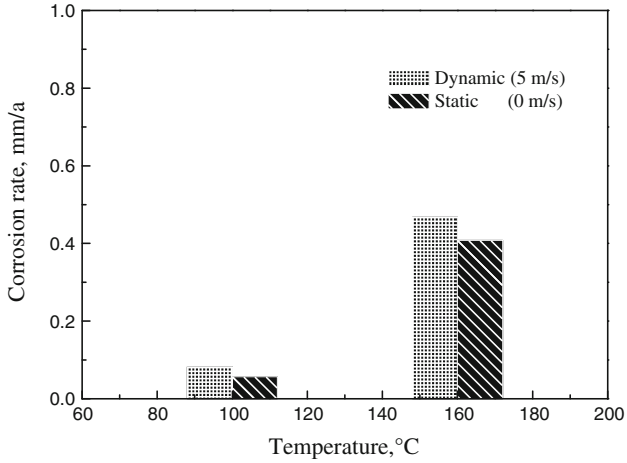

Fig. 2 Corrosion rates of 13Cr stainless steel obtained under the dynamic/static flow condition at 100 and 160 °C

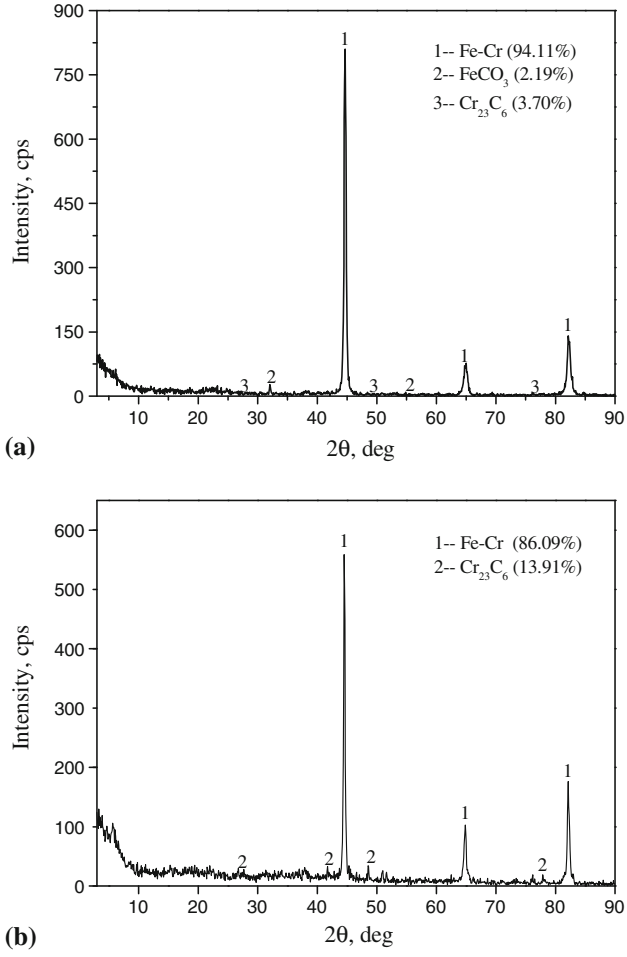

Fig. 3 XRD spectra of corrosion product layers formed under the dynamic flow condition at 100 and 160 °C

The turbulent flow interferes with the formation of corrosion product layers (or passive films) and peels them away at some localized sites, resulting in the difference in corrosion rates at 100 or 160 °C. It is in agreement with the corrosion morphologies as described above. It is worthwhile to consider that the

corrosion rate increases probably to certain maximum beyond temperatures in the tests. This is a fact that the maximum of corrosion rate depends on the equilibrium between precipitation and dissolution of corrosion products layers. In deed, the amount of scales retained on the steel surface at any point in time depends on the balance of scale formation (generated by precipitation from the solution) and scale damage (by hydrodynamic stress and the chemical dissolution).

3.2 XRD and XPS analyses

XRD spectra of the corrosion product layers on 13Cr stainless steel are showed in Fig. 3. XRD spectra reveal that the main phases in all corrosion scales are Fe-Cr compound, limited amount of iron carbonate ($FeCO_3$) and a few $Cr_{23}C_6$ at 100 °C. In contrast, Fig. 3(b) shows that at 160 °C the corrosion products layers are principally composed of Fe-Cr compound, with a little amount of $Cr_{23}C_6$. The efficient Cr content decreases with temperature from 100 to 160 °C based on the peaks intensities as shown in Fig. 3.

XPS peaks spectra and the corresponding fitting peaks spectra are shown in Fig. 4, in which the spectra of special interest are Fe 2p, Cr 2p, O 1s, and C 1s. The BEs of these elements in corrosion films are well detected. Figure 4(a) shows survey spectrum of the corrosion film on sample surface. The C 1s high-resolution XPS scans in Fig. 4(a) reveal three peaks at the BEs of 284.47, 286.01, and 288.89 eV. The first peak at 284.47 eV close to 284.6 eV corresponds to $Cr_{23}C_6$ absorbed in corrosion product layer, while the third peak at 288.89 eV around 289.6 eV is attributed to pure iron carbonate (Ref 26). However, the third C 1s peak is the undefined substance due to the complex compound or imprecise fitting. Figure 4(b) presents the O 1s high-resolution XPS spectra of the corrosion product layer, in which the peaks at BE 529.57, 531.61, and 533.16 eV correspond to CrO, $Cr(OH)_3$, and $FeCO_3$, respectively. The oxides presented in the passive layer can be explained due to short time exposure in air prior to XPS analysis.

Figure 4(c) shows the XPS spectra for Cr 2p region in corrosion film. It can be seen that there is one peak for Cr 2p spectra at 575.77 eV and a satellite peak at 572.93 eV. The CrO oxide formed in corrosion product layer corresponds to the BE around 575.77 eV, which is probably attributed to the decomposition of the corrosion product $Cr(OH)_3$. However, compounds with respect to the satellite peak are uncertain in this corrosive system. The fitting peaks in Fe $2p_{3/2}$ region for 13Cr stainless steel are presented in Fig. 4(d), where the corresponding BE and intensities are depicted. The first peak at 706.02 eV can be either due to the exposure of metal substrate, the presence of uncorroded metal in film layer, or modification of the oxidation states to lower value of various components that may occur during the sputtering process, which was suggested by Lopez et al. (Ref 27). An examination of Fe 2p spectra reveals that the peak at 708.70 eV evidences the presence of $FeCO_3$ deposit. In addition, the peak around 712.64 eV may be the characteristics of the compound FeO(OH)-Fe_2O_3. The oxide formation of Fe_2O_3 is attributed to the decomposition of $FeCO_3$, in despite of the formation of corrosion film under

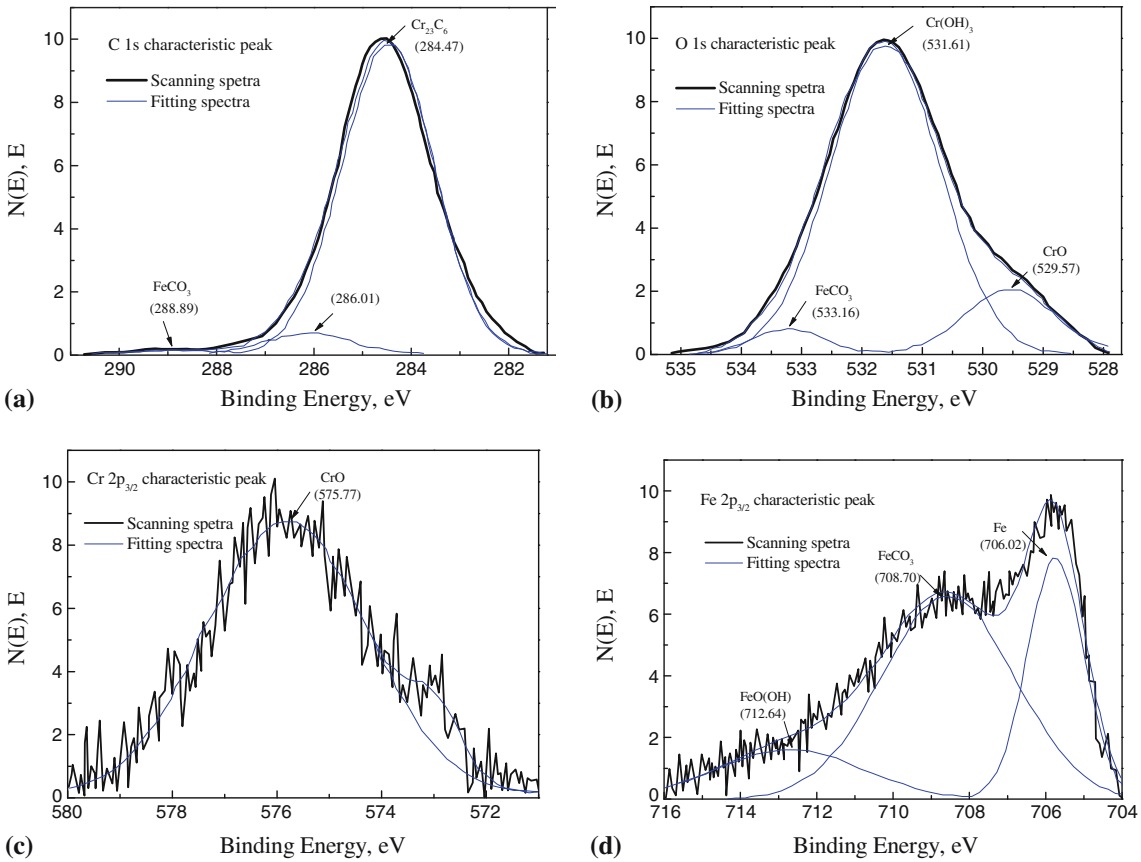

Fig. 4 XPS fitting peaks spectra of corrosion product layers at 100 °C under the dynamic flow condition: (a) C 1s characteristic peak, (b) O 1s characteristic peak, (c) Cr $2p_{3/2}$ characteristic peak and (d) Fe $2p_{3/2}$ characteristic peak

deoxidized solution. On the other hand, it can be explained considering that the oxide forms over the exposure of corroded sample to dried atmosphere prior to the XPS analysis. The overall XPS spectra indicate that the oxides formation contributes to corrosion resistance of the protective film in aggressive oilfield conditions.

3.3 Cyclic Potentiodynamic Polarization

Figure 5 shows the effect of Cl^- ion concentration on cyclic potentiodynamic polarization curve of 13Cr stainless steel in simulated oilfield brine at various temperatures. The significant pitting parameters such as natural corrosion potential (E_{corr}), pitting potential (E_{pit}), protection potential (E_{pp}), ΔE (the difference between E_{pit} and E_{pp}), and passive current density (I_{pass}) in cyclic polarization curves at various temperatures are shown in Fig. 5b. It can be seen that the pitting potential (E_{pit}) and the protection potential (E_{pp}) shift in the negative direction with the increase of temperature, indicating that temperature has an important effect on the susceptibility of pitting corrosion. However, there are not well linear relationships for E_{pit} and E_{pp} as a function of temperature. The difference between the pitting potential and the pit repassivation potential for the corrosion system can be defined as the relative corrosion resistance, i.e. $\Delta E = E_{pit} - E_{pp}$. The magnitude of ΔE is considered as an indicator for pitting resistance, i.e., the higher the ΔE value, the lower the pitting resistance (Ref 28, 29). The values of ΔE are, respectively, 0.227, 0.237, and 0.220 V at 30, 60, and 90 °C, but they do not reflect the relation above.

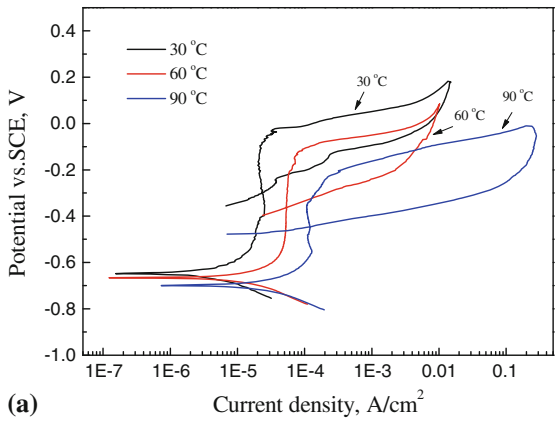

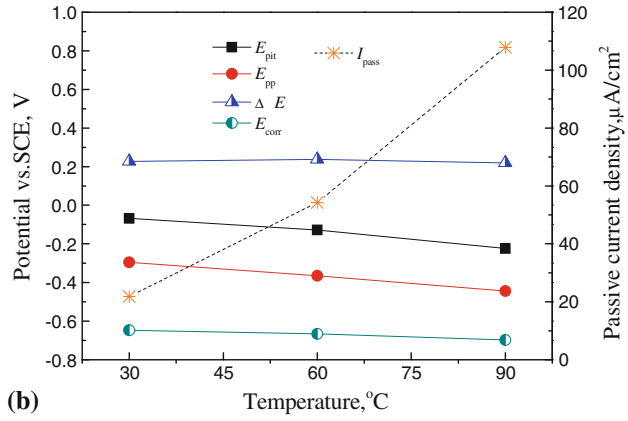

Fig. 5 Effect of temperature on the cyclic potentiodynamic polarization of 13Cr stainless steel in simulated solution: (a) polarization curves and (b) variables of E_{pit}, E_{pp}, E_{corr}, ΔE, and I_{pass}

In addition, it is clear that the natural corrosion potential (E_{corr}) shifts slightly in the negative direction with increasing temperature. The passive current density (I_{pass}) increases with temperature, which indicates that increased temperature accelerates the reaction activity and reduces pitting resistance.

During the passivation process, the metal involves in three processes. Active anodic dissolution process can be expressed as

$$Fe + H_2O \rightarrow (FeOH)_{ad} + H^+ + e \quad \text{(Eq 1)}$$

then,

$$(FeOH)_{ad} \rightarrow FeOH^+ + e \quad \text{(Eq 2)}$$

$$FeOH^+ + H^+ \rightarrow Fe^{2+} + H_2O \quad \text{(Eq 3)}$$

After the active anodic dissolution in Eq 3, the passivation reactions can be written by

$$(FeOH)_{ad} + H_2O \rightarrow [Fe(OH)_2]_{ad} + H^+ + e \quad \text{(Eq 4)}$$

$$[Fe(OH)_2]_{ad} \rightarrow FeO + H_2O \quad \text{(Eq 5)}$$

where FeO is the formed passivation film substance. Here, we do not consider other oxide film such as Cr_2O_3 for simplification. Once the passivation film has formed, the oxide substance begins to dissolve in the solution to form the active ferrous ions, as presented in Eq 6

$$FeO + 2H^+ \rightarrow Fe^{2+} + H_2O \quad \text{(Eq 6)}$$

It can be easily understood that the passivation process is determined by combined effect between passive film formation and passive film dissolution. Because the simulated oilfield brine contains high Cl^- concentration, Cl^- ions will react with metal ions to form complex compound leading to more rapid dissolution of oxide film and even the formation of corrosion pits. The complex reaction can be expressed as follows:

$$FeO + 2Cl^- + 2H^+ \rightarrow FeCl_2 + H_2O \quad \text{(Eq 7)}$$

4. Conclusions

Temperature and flow rate had a significant effect on characterization of corrosion product layers or passive films formed on 13Cr stainless steel. At high temperature such as at 160 °C, lots of corrosion micro-pits were formed on the localized sites of corrosion product layers. Corrosion rates under the condition of 5 m/s were higher than those under the static flow condition at 100 or 160 °C.

Corrosion product layers were mainly composed of Fe-Cr compound, limited amount of iron carbonate ($FeCO_3$) and a few $Cr_{23}C_6$ precipitates as revealed by x-ray diffraction. XPS analysis showed that that there were some other compounds such as CrO, $Cr(OH)_3$, and FeO(OH) in the corrosion product layers.

The corrosion parameters such as E_{corr}, E_{pit}, and E_{pp} shifted in the negative direction with an increase in temperature. In addition, the value of ΔE and I_{pass} also showed the pitting behavior of 13Cr stainless steel at various temperatures. As temperature increased, the pitting susceptibility of 13Cr stainless steel was increased.

Acknowledgments

The authors gratefully acknowledge financial support by Key Laboratory Opening Fund (No. 06A40302) of Corrosion and Protection of Tabular Goods Research Center of China National Petroleum Corporation and Petroleum Research Institute of Shaanxi Yanchang Petroleum Group Company.

References

1. D.S. Carvalho, C.J.B. Joia, and O.R. Mattos, Corrosion Rate of Iron and Iron-Chromium Alloys in CO-Medium, *Corros. Sci.*, 2005, **47**, p 2974–2986
2. B.R. Linter and G.T. Burstein, Reactions of Pipeline Steels in Carbon Dioxide Solutions, *Corros. Sci.*, 1999, **41**, p 117–139
3. E. Dayalan, F.D. Moraes, J.R. Shadley, S.A. Shirazi, and E.F. Rybicki, *CO_2 Corrosion Prediction in Pipe Flow Under $FeCO_3$-Forming Conditions, Corrosion/98*, NACE International, Houston, TX, 1998, Paper no. 51
4. D.A. Lopez, T. Perez, and S.N. Simison, The Influence of Microstructure and Chemical Composition of Carbon and Low Alloy Steels in CO_2 Corrosion. A State-of-art Appraisal, *Mater. Des.*, 2003, **24**, p 561–575
5. K. Masamura, S. Hashizume, Y. Inohara, and Y. Minami, *Estimation Models of Corrosion Rates of 13% Alloys in CO_2 Environments, Corrosion/99*, NACE International, Houston, TX, 1999, Paper no. 583
6. K. Denpo and H. Ogawa, Fluid Flow Effects on CO_2 Corrosion Resistance of Oil Well Materials, *Corrosion*, 1993, **49**(6), p 442–449
7. T. Hara, H. Asahi, Y. Suehiro, and H. Kaneta, Effect of Flow Velocity on Carbon Dioxide Behavior in Oil and Gas Environments, *Corrosion*, 1994, **56**(8), p 860–866
8. J.M. Bastidas, C.L. Torres, E. Cano, and J.L. Polo, Influence of Molybdenum on Passivation of Polarized Stainless Steels in a Chloride Environment, *Corros. Sci.*, 2002, **44**, p 625–633
9. R.C. Newman, Understanding the Corrosion of Stainless Steel, *Corrosion*, 2001, **57**, p 1030–1041
10. M.S. Cayard and R.D. Kane, *Corrosion Degradation Mechanism in Coiled Tubing. Corrosion/98*, NACE International, Houston, TX, 1998, Paper no. 112
11. S. Hashizume, T. Takaoka, Y. Minami, and Y. Ishizawa, *Corrosion Resistance and Mechanical Properties of High-Strength 15%Cr Stainless Steel for OCTG, Corrosion*/95, NACE International, Houston, TX, 1995, Paper no. 78
12. Y. Miyata, Y. Yamane, O. Furukimi, H. Niwa, and K. Tamaki, *Corrosion of New 13Cr Stainless Steel OCTG in Severe CO_2 Environment, Corrosion/95*, NACE International, Houston, TX, 1995, Paper no. 83
13. M.B. Kermani, G. Weighhill, T. Pendlington, and G. Elliot, *Operational Experience of Using 13%Cr Tubular Steels, Corrosion/95*, NACE International, Houston, TX, 1995, Paper no. 96
14. K. Videm and A. Dugstad, Corrosion of Carbon Steel in an Aqueous Carbon Dioxide Environment, Part 1: Solution effects, *Mater. Perform.*, 1989, **28**, p 64
15. C.Y. Chao, L.F. Lin, and D.D. Macdonald, A Point Defect Model for Anodic Passive Films, *J. Electrochem. Soc.*, 1981, **128**, p 1187–1194
16. D. Bauernfeind and G. Mori, *Corrosion of Superaustenitic Stainless Steels in Chloride- and Sulfate-Containing Media—Influence Of Alloying Elements Cr, Mo, N and Cu, Corrosion/03*, NACE International, Houston, TX, 2003, Paper no. 257
17. J.O. Park, S. Matsch, and H. Bohni, Effect of Temperature and Chloride Concentration on Pit Initiation and Early Pit Growth of Stainless Steel, *J. Electrochem. Soc.*, 2002, **149**, p B34–B39
18. A. Ikeda, M. Ueda, and S. Mukai, *CO_2 Corrosion Behavior and Mechanism of Carbon Steel and Alloy Steel, Corrosion/83*, NACE International, Houston, TX, 1983, Paper no. 45
19. H.S. Isaacs and G. Kissel, Surface Preparation and Pit Propagation in Stainless Steels, *J. Electrochem. Soc.*, 1972, **119**, p 1628–1632
20. B.E. Wilde and E. Willianms, The Relevance of Accepted Electrochemical Pitting Tests to Long-Term Pitting and Crevice Corrosion Behavior of Stainless Steels in Marine Environments, *J. Electrochem. Soc.*, 1971, **118**, p 1057–1062
21. Z. Szklarska-Smialowska, *Pitting Corrosion of Metals*, National Association of Corrosion Engineers, Houston, 1986, p 351
22. D.A. Jones, *Principles and Preventions of Corrosion*, Macmillan Publishing Company, New York, 1992
23. G. Schmitt, *Fundamental Aspect of CO_2 Corrosion, Corrosion/84*, NACE International, Houston, TX, 1984, Paper no. 10
24. K. Videm, *Fundamental Studies Aimed at Improving Models for Prediction of CO_2 Corrosion, Corrosion/2000*, NACE International, Houston, TX, 2000, Paper no. 39
25. X.P. Guo and Y. Tomoe, Electrochemical Behavior of Carbon Steel in Carbon Dioxide Saturated Diglycolamine Solutions, *Corrosion*, 1998, **54**(11), p 931
26. J.K. Heuer and J.F. Stubbins, An XPS Characterization of $FeCO_3$ Films from CO_2 Corrosion, *Corros. Sci.*, 1999, **41**, p 1231–1243
27. D.A. Lopez, W.H. Schreiner, S.R. de Sanchez, and S.N. Simison, The Influence of Carbon Steel Microstructure on Corrosion Layers. An XPS and SEM Characterization, *Appl. Surf. Sci.*, 2003, **207**, p 69–85
28. B.E. Wilde, A Critical Appraisal of Some Popular Laboratory Electrochemical Tests for Predicting the Localized Corrosion Resistance in Sea Water, *Corrosion*, 1972, **28**, p 283–291
29. H.P. Leckie and H.H. Uhlig, Environmental Factors Affecting the Critical Potential for Pitting 18-8 Stainless Steel, *J. Electrochem. Soc.*, 1966, **113**, p 1262–1267